



OPEN

## A comparative study of target fabrication strategies for microgram muonic atom spectroscopy

L. Antwis<sup>1</sup>, S. Bara<sup>2</sup>, C. Bruhn<sup>3</sup>, T. E. Cocolios<sup>2</sup>, M. Deseyn<sup>2</sup>, A. Doinaki<sup>4,5</sup>, Ch. E. Düllmann<sup>3,6,7</sup>, J. Fletcher<sup>1</sup>, M. Heines<sup>2</sup>✉, R. Heller<sup>8</sup>, P. Indelicato<sup>9</sup>, U. Kentsch<sup>8</sup>, T. Kieck<sup>6,7</sup>, K. Kirch<sup>4,5</sup>, A. Knecht<sup>5</sup>, E. A. Maugeri<sup>10</sup>, M. Niikura<sup>11</sup>, A. Ouf<sup>12</sup>, L. M. C. Pereira<sup>13</sup>, W. W. M. M. Phy<sup>2</sup>, R. Pohl<sup>12,14</sup>, D. Renisch<sup>3,6</sup>, N. Ritjoh<sup>15</sup>, A. Vantomme<sup>13</sup>, S. M. Vogiatzi<sup>2</sup>, K. von Schoeler<sup>4</sup>, F. Wauters<sup>14,16</sup>, A. Zendour<sup>4,5</sup> & S. Zweidler<sup>4</sup>

Muonic atom spectroscopy is a method that can determine absolute nuclear charge radii with typical relative precision of  $10^{-3}$ . Recent developments have enabled to extend muonic atom spectroscopy to microscopic target quantities as low as 5  $\mu\text{g}$ . This substantial reduction from the traditional limit of the order of 100 mg is based on a transfer mechanism in a high-pressure hydrogen gas cell, which transports the muon to the surface of the target material rather than stopping it over a broad depth range. This approach enables the measurement of absolute nuclear charge radii of long-lived radioactive isotopes (half-life above  $\sim 20$  years), but the production of appropriate targets for the technique has presented some major challenges, such as the formation of organic layers on the substrate. This study presents a systematic investigation of the stopping efficiency for different target preparation methods: ion implantation, drop-on-demand printing, and molecular plating. Notable differences between the three methods were discovered in terms of their performance allowing to further fine tune the method of choice for future target preparations. Our findings show that implantation provides appropriate targets for our method with negligible losses. This achievement opens the landscape of potential measurements to isotopes where high mass separation is required not achievable with other methods. Furthermore, molecular plated targets performed substantially better than those prepared using drop-on-demand printing.

Muonic atom spectroscopy exploits the distinctive properties of the muon in order to study the atomic nucleus. The muon is a lepton with a mass approximately 207 times larger than that of the electron. When negative muons are brought close to a nucleus, the Coulomb attraction can lead to the formation of a *muonic atom*. One can understand the main differences between regular atoms and muonic atoms by replacing the mass of the electron by that of the muon in the Bohr model. Due to the large muon-to-electron mass ratio, the atomic binding energy is much higher than for electrons, while the Bohr radius is severely reduced compared to its electronic counterparts (both approximately by a factor  $m_\mu/m_e \approx 207$ ). Because of their reduced distance to the nucleus, muonic atoms are much more sensitive to nuclear finite size effects, by a factor  $(m_\mu/m_e)^3 \approx 10^7$ . This enhanced sensitivity forms the cornerstone of the muonic atom spectroscopy method. Unlike other atomic spectroscopy methods, which primarily probe changes in mean square radii via the isotope shift<sup>1</sup>, muonic atom

<sup>1</sup>Ion Beam Centre, University of Surrey, Guildford, UK. <sup>2</sup>Institute for Nuclear and Radiation Physics, KU Leuven, Leuven, Belgium. <sup>3</sup>Department of Chemistry, Johannes Gutenberg University Mainz, Mainz, Germany. <sup>4</sup>Institute for Particle Physics and Astrophysics, ETH Zürich, Zurich, Switzerland. <sup>5</sup>PSI Center for Neutron and Muon Sciences, Villigen, Switzerland. <sup>6</sup>Helmholtz Institute Mainz, Mainz, Germany. <sup>7</sup>GSI Helmholtzzentrum für Schwerionenforschung GmbH, Darmstadt, Germany. <sup>8</sup>Helmholtz-Zentrum Dresden-Rossendorf, Dresden, Germany. <sup>9</sup>Laboratory Kastler Brossel, Sorbonne University, CNRS, ENS-PSL Research University, Collège de France, Paris, France. <sup>10</sup>PSI Center for Nuclear Engineering and Sciences, Villigen, Switzerland. <sup>11</sup>RIKEN Nishina Center, Wako, Saitama, Japan. <sup>12</sup>Institute of Physics, QUANTUM, Johannes Gutenberg University Mainz, Mainz, Germany. <sup>13</sup>Quantum Solid-State Physics, KU Leuven, Leuven, Belgium. <sup>14</sup>PRISMA+ Cluster of Excellence, Johannes Gutenberg University Mainz, Mainz, Germany. <sup>15</sup>Suranaree University of Technology, Nakhon Ratchasima, Thailand. <sup>16</sup>Institute of Nuclear Physics, Johannes Gutenberg University Mainz, Mainz, Germany. ✉email: michael.heines@kuleuven.be

spectroscopy allows to extract the absolute nuclear mean square charge radii directly from transition energies of the corresponding x rays. These absolute radii provide invaluable input for benchmarking radii attained from other techniques, such as laser spectroscopy, thus enhancing their precision<sup>2</sup>. An external input that is still required is the shape of the nucleus. This input can be extracted from elastic electron scattering, recent advancements of which show the feasibility of measurements on long-lived radioactive species<sup>3</sup>.

A central challenge in muonic atom spectroscopy lies in the formation of these exotic atoms. To capture a muon in the Coulomb potential of a nucleus, the muon's energy must be at most a few electronvolt. Traditional methods rely on the direct stopping in the target material of interest. However, given the typical momentum of negative muon beams at accelerator facilities, the stopping range is of the order of a millimeter. Hence, the required amount of target material is typically at least  $\mathcal{O}(100)$  mg, corresponding to a target thickness of about 100  $\mu\text{m}$  – 1 mm, depending on the target material. In the case of isotopically pure or radioactive samples, this is often not achievable.

Recent developments introduced a high-pressure hydrogen gas cell (100 bar) with a small deuterium admixture ( $\sim 0.25\%$ ) in order to slow down muons sufficiently for atomic capture on the surface of a substrate<sup>4</sup>. First, the muon is stopped in a gas target of 100 bar  $\text{H}_2$  with a small deuterium admixture, forming muonic hydrogen ( $\mu\text{p}$ ) in the process. The muonic hydrogen atom will diffuse in the gas cell with a very short mean free path, until it encounters a deuterium atom. As the binding energy for a muon to the deuteron is slightly higher than that of the proton, the muon is transferred, such that muonic deuterium ( $\mu\text{d}$ ) is formed. Due to the Ramsauer-Townsend minimum in the scattering cross section of  $\mu\text{d}$  in  $\text{H}_2$ <sup>5</sup>, the  $\mu\text{d}$  observes an almost transparent gas cell, such that a large fraction of them can diffuse to the end of the gas cell, transferring the muon to the nucleus of interest. A schematic representation of the transfer process is shown in Fig. 1. This method reduces the required target material to approximately 5  $\mu\text{g}$ , opening the door to studies with long-lived radioactive isotopes ( $\tau_{1/2} \gtrsim 20$  years), as well as rare isotopes that are not available in larger quantities. The half-

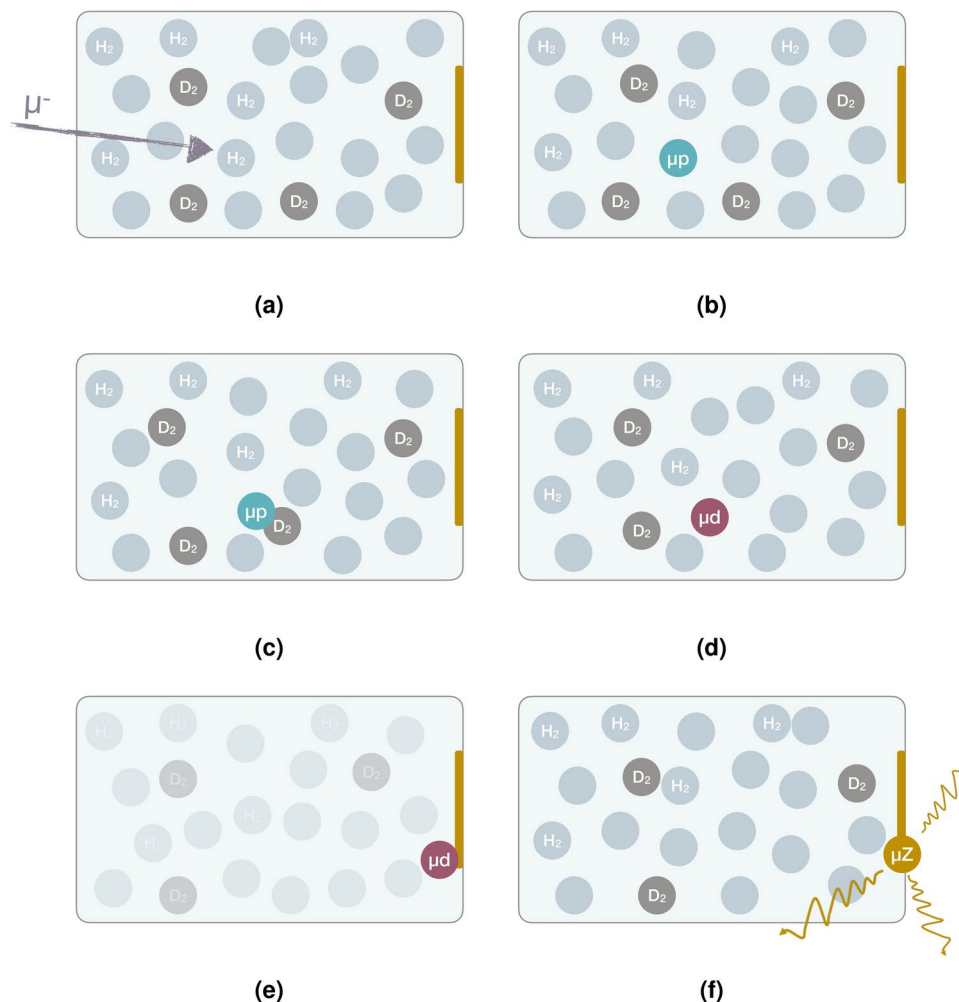


**Fig. 1.** Schematic representation of the transfer process explained above. (a) Muon enters the gas cell, (b) muon is stopped and forms  $\mu\text{p}$ , (c)  $\mu\text{p}$  diffuses until it gets close to  $\text{D}_2$ , (d) muon is transferred to deuterium, (e)  $\mu\text{d}$  diffuses to the back of the gas cell, (f) muonic atom of interest is formed and corresponding x rays are emitted<sup>6</sup>.

life limitation is at this time primarily limited by radioprotection limits and gamma background in the detector array emanating from the target.

This work aims to build on previous developments by investigating the muonic x-ray yields for different target production methods. First, the attenuation of the diffusing  $\mu d$  atoms through different layer thicknesses of graphite was investigated. The goal of these measurements was to show the feasibility of using implanted targets, and to probe the optimal implantation depth for measurements. This optimal depth still has to be combined with implantation limitations, which are specific to the implanted species of interest. Furthermore, the range of  $\mu d$  atoms provides an indication of the importance of thin layers of organic material being present on top of the substrate. These organic layers may often form on top of substrates during chemical preparation, originating from the solutions used for the target preparation or contact with air. Next, samples implanted with gold or potassium were investigated and compared to surface deposited targets of similar masses. Gold is used as a benchmark for heavy elements, as it is stable and mono-isotopic.  $^{39}\text{K}$ , on the other hand, was measured as a test for a future measurement on  $^{40}\text{K}$ . For potassium, metallic surface deposition is not possible. Hence, chromium surface targets were used as a proxy. Finally, a comparison was made between barium targets prepared using molecular plating (MP)<sup>7–9</sup> and drop-on-demand printing (DoD)<sup>10</sup>, both of which stand at the forefront of radioactive target development.

## Methods

### Experimental setup

The systematic study was performed at the  $\pi\text{E1}$  beamline of the Paul Scherrer Institute's High Intensity Proton Accelerator (HIPA) facility<sup>11</sup>. Figure 2a shows the experimental apparatus used for this study. A set of scintillators is used for coincidence and veto logic. The first type is a muon veto, which collimates the beam and vetoes background outside of the acceptance of the gas cell. Downstream of this veto detector, a muon entrance detector is positioned. The main purpose of this detector is to relate the timing of measured x rays to the muon's arrival time, such that the background can be substantially reduced using coincidence logic. Finally, a set of electron veto scintillator detectors is placed around the gas cell in order to detect Michel electrons (electrons originating from muon decay). By using these as veto signals, direct hits of these electrons on the germanium detectors and Bremsstrahlung generated by them can be substantially reduced.

The targets are placed at the back of a high-pressure gas cell made of aluminium, which is in turn closed off towards the muon beamline using a 600  $\mu\text{m}$ -thick carbon fiber window. To withstand a pressure of 100 bar, a titanium and carbon fiber support grid was added. This entrance window of the gas cell has a transmission of about 55% for muons, as shown in Ref.<sup>4</sup>. The gas injection is handled in a similar way as in some of our previous work<sup>4</sup>. A CAD drawing of the gas cell is shown in Fig. 2b.

An array of germanium detectors of various types is placed around the gas cell for the detection of the muonic x rays. The array was constructed together with the MIXE collaboration<sup>12</sup>. The detectors in the frame consisted of a Miniball cluster detector<sup>13</sup>; a telescope (coax + planar crystals); reverse electrode coaxial germanium (REGe) detectors with relative efficiencies of 95% (x1), 70% (x2), and 60% (x1); standard electrode coaxial germanium (SEGe) detectors with relative efficiencies of 50% (x3) and 75% (x1), and broad energy germanium (BEGe) detectors (x5).

The data acquisition was performed using SIS3316 digitizer modules from Struck Innovative Systeme. The modules have 16 channels each, with a sampling rate of 250 MHz. The outputs of the plastic scintillators and germanium detectors were saved without hardware triggers, such that coincidence and veto logic could be applied offline after optimization. The energy determination of the germanium detectors was extracted from a trapezoidal filter on field programmable gate arrays (FPGAs) onboard of the digitizer modules. Besides the trigger time and energy, the first 1.2  $\mu\text{s}$  (300 samples) are also saved in order to calculate improved timestamps, as explained in the analysis methods section.

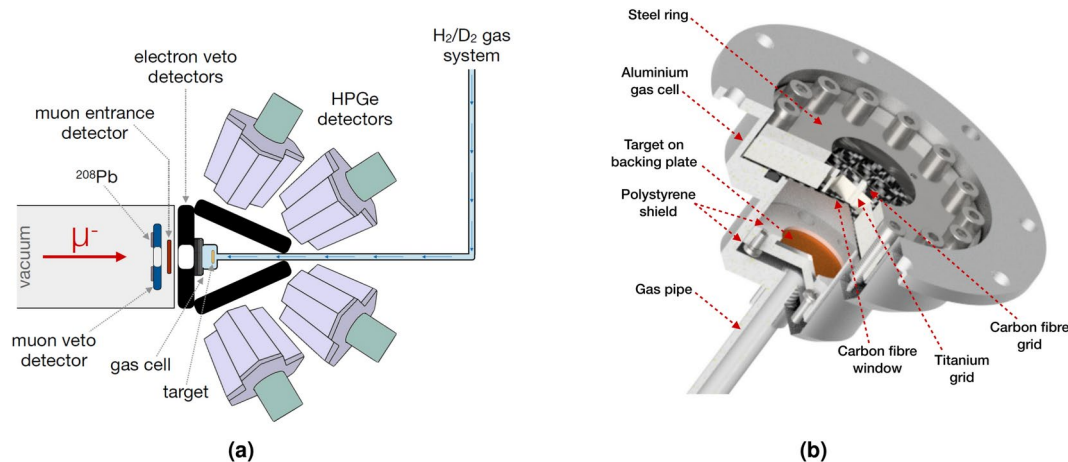


**Fig. 2.** Schematic of the setup<sup>4</sup> (left) and CAD drawing of the gas cell<sup>16</sup> (right).

### Sample preparation

As a backing material, glassy carbon (SIGRADUR K) disks with a thickness of 1 mm and a diameter of 16 mm were purchased from Hochtemperatur-Werkstoffe GmbH. This material is a high-purity porous form of carbon with greater strength and surface quality than graphite. A low-Z material is preferred for the backing material, such that no muonic x-ray background is generated in the energy regions of interest. Furthermore, for the implanted targets, such materials should display less sputtering than higher proton number alternatives. Over the years, gold has become the reference for optimization of the setup. The primary reason for this is that it is mono-isotopic while being available in many different forms. Consequently, it was the isotope of interest chosen to investigate the attenuation of the x-ray signal through graphite and as a first proof of principle for implanted targets. Additionally, implanted targets of  $^{39}\text{K}$  were prepared as a test for a future campaign evaluating  $^{39}$ ,  $^{40}$ ,  $^{41}\text{K}$ , where  $^{40}\text{K}$  can only be attained at a sufficient purity through magnetic mass separation. A measurement of such a triplet could be used to benchmark existing laser spectroscopy experiments<sup>14</sup>. Finally, drop-on-demand and molecular plating targets of barium were prepared. Barium is a homologue of radium, for which the charge radius measurement is a key goal of our program<sup>15</sup>.

In the interest of having reference targets to compare to the implanted targets, we prepared several targets using physical vapor deposition. The first set of targets was prepared by evaporating the material under vacuum in a tungsten crucible heated electrically. The resulting targets had 50, 10, and 3 nm thick gold layers, amounting to 170, 34, and 10  $\mu\text{g}$  and a 25 and 4 nm chromium target (32 and 5  $\mu\text{g}$ ). The 50 nm target served for optimization purposes, while the others acted as a reference for the gold and the potassium (chromium being reasonably close in Z to potassium) implanted targets, respectively. Additionally, we prepared targets via DC magnetron sputtering in an Ar atmosphere. They consisted of a 50 nm gold layer (thick enough such that all the  $\mu\text{d}$  atoms that reach it transfer to gold) and a layer of graphite on top (0, 10, 25, 50, 100, 250 nm).

To evaluate implanted targets produced at different implantation energies, glassy carbon disks were implanted with stable  $^{197}\text{Au}$  at 4.5, 27, and 90 keV at the UK National Ion Beam Centre in Surrey. These energies were initially chosen to correspond to projected ranges of 10, 25, and 50 nm as predicted by SRIM<sup>16</sup>. However, due to sputtering effects, this range can be substantially be reduced<sup>17,18</sup>. Similarly, a 30 keV implantation of the stable  $^{39}\text{K}$  on glassy carbon was performed at Helmholtz-Zentrum Dresden-Rossendorf (HZDR). In order to investigate self-sputtering, where earlier implanted atoms are removed from the sample by implanting new ions, TRIDYN<sup>19</sup> simulations were performed. Rutherford backscattering spectrometry (RBS) was performed as verification of the simulations. These measurements did not fully match our observations, likely due to a combination of the porosity of glassy carbon and off-diagonal elements in the surface binding energy matrix. A more detailed discussion of these simulations can be found in Ref.<sup>17</sup>. The RBS profile for the implanted potassium sample is shown in Fig. 3. From this spectrum, one can see that there is a substantial low-energy tail for potassium (deeper in the substrate). This tail is most likely caused by the high reactivity of potassium and/or temperature-induced diffusion in the sample during implantation. Consequently, only about 60% of the particles are located near the surface of the substrate. Furthermore, there is a large peak in the spectrum originating from oxygen (not present before implantation). We suspect that this is primarily caused by the strong reactivity of elemental potassium.

In order to evaluate the different chemical target preparation techniques, drop-on-demand (DoD) and molecular plating (MP) samples were prepared on glassy carbon backing with deposition masses of 5, 10, 25, and 50  $\mu\text{g}$ . Due to a tight experimental schedule and a clear global conclusion, the 5  $\mu\text{g}$  DoD target and the 50  $\mu\text{g}$  MP target were not measured. The molecular plated samples were prepared with the setup described in Ref.<sup>7</sup>. The sample preparation was performed in galvanostatic mode. MP parameters, such as voltage, current density and deposition time were defined to maximize the deposition yield while producing thin, uniform and homogeneous films. By using trace amounts of the radioactive  $^{133}\text{Ba}$ , the homogeneity and yield could be monitored. Radiographic imaging, as shown in Fig. 4 (left), indicates a homogeneous spatial distribution over the entire surface, except for the edges. The DoD samples were prepared using the method described in Ref.<sup>10</sup>. A commercial Ba ICP-MS-standard solution with a concentration of  $1 \mu\text{g } \mu\text{L}^{-1}$  was used as stock solution. This stock solution was evaporated and subsequently redissolved in 0.5 M  $\text{HNO}_3$  and diluted with acetonitrile. The following printing sequence was used: 261 drops, 20 nL each, in a circular pattern with a diameter of 10 mm

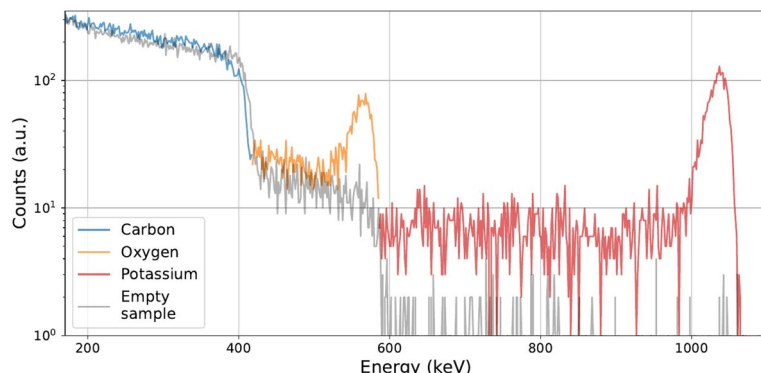


**Fig. 3.** RBS spectrum for an empty glassy carbon sample (grey) and implanted  $^{39}\text{K}$  target (color). The data was obtained using an incident  $1.57 \text{ MeV}^4\text{He}^+$  beam and a detector placed at a scattering angle of  $161.5^\circ$ .

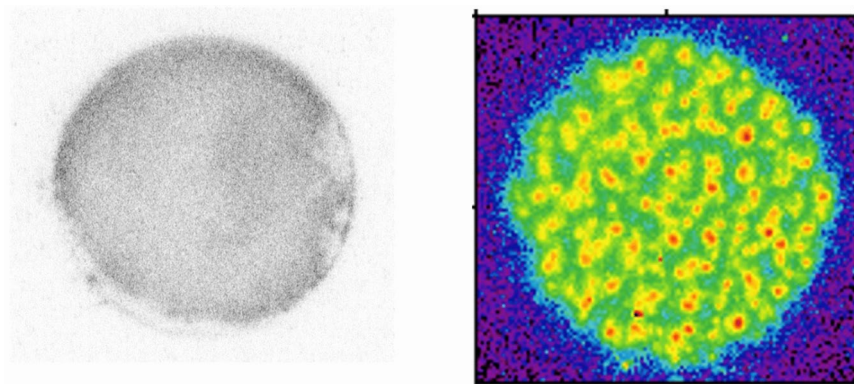


**Fig. 4.** Radiography images of one of the MP samples (left) and one of the DoD samples (right). Apart from the sample edges, the MP sample shows an excellent homogeneity. The DoD sample, on the other hand, shows some clustering.

Method	Targets
Surface deposition	Au (50/10/3 nm)
	Cr (25/4 nm)
	Au + C (50 nm + 0/10/25/50/100/250 nm)
Implantation	Au (4.5/27/90 keV)
	K (30 keV)
Molecular plating	Ba (5/10/25/50 $\mu$ g)
Drop-on-demand	Ba (5/10/25/50 $\mu$ g)

**Table 1.** Overview of the 23 targets prepared using different techniques.

This results in a deposition of 5.22  $\mu$ L of the solution, which corresponds to 5.22  $\mu$ g of Ba. For the PipeJet printer by BioFluidix, the tip size “200-L” was used, at a stroke velocity of 75  $\mu$ m ms<sup>-1</sup>. In order to produce 4 targets with different amounts of Ba, this sequence was printed once (5  $\mu$ g Ba), twice (10  $\mu$ g Ba), five times (25  $\mu$ g Ba), and ten times (50  $\mu$ g Ba) on the individual glassy carbon backings. These backings were cleaned with deionized water, isopropanol and acetone before usage. Similar to the MP samples, radiography was performed to check the sample homogeneity. This time, stable <sup>130</sup>Ba was irradiated with neutrons before printing to artificially induce radioactivity in the sample. The radiographic image, as shown in Fig. 4 (right), indicated that the activity is distributed along the substrate, but there are localized clusters of higher concentrations. These clusters were further investigated using scanning electron microscopy (SEM), which showed micocrystallites formation around the radioactivity hotspots, which is not favored for microgram muonic atom experiments. An overview of the targets used for this study is given in Table 1.

### X-ray intensities

In this study, we investigated the quality of targets by evaluating the observed intensity of the  $2p_{1/2}-1s_{1/2}$  and  $2p_{3/2}-1s_{1/2}$  transitions in the muonic atoms of interest (<sup>39</sup>K, <sup>52</sup>Cr, <sup>138</sup>Ba, and <sup>197</sup>Au). These lines are the most important, as they have a high intensity and display the strongest effect due to finite size effects. In order to transform count rates to atomic capture rates, the corresponding x-ray intensities are needed. Calculations for these intensities were performed using the muon cascade program developed by Akylas and Vogel<sup>20</sup>. The input parameters for this code include the atomic mass and the electronic binding energies for the K, L and M orbits, as referenced in Ref.<sup>21–23</sup>, as well as the effective nuclear charge for the same electronic shells<sup>24,25</sup>. Additionally, the transition energies for  $2p-1s$  and  $2s-2p$  in the muonic atoms were calculated using Mudirac<sup>26</sup>, and used as an input for the cascade code. Mudirac typically reproduces the experimental  $2p-1s$  transition energies with a reliability of 0.1%. Therefore, the extracted transition energies are deemed sufficiently precise for calculations on the x-ray intensity.

The cascade code also requires information about the electronic filling fraction of the K, L, and M shells, along with the principal quantum number  $n$ , which indicates the starting point of the muon cascade. Another important input is the distribution of muons over the orbital angular momentum states. The initial distribution of muons in the atomic levels after their capture via transfer, denoted as ( $n_{\text{initial}}$  and  $Pl_{\text{initial}}$ ), deviates from the typically assumed statistical distribution after the muon's direct atomic capture where  $n_{\text{initial}} \approx 14$  and  $Pl_{\text{initial}} = (2l + 1)$ . The ( $n_{\text{initial}}$  and  $Pl_{\text{initial}}$ ) after transfer are calculated based on the formulas presented in Ref.<sup>27</sup>.

The aforementioned parameters are believed to be well under control. The main unknown in the cascade simulation is the refilling rate of the electronic K-shell after Auger emissions. Following the findings in<sup>28,29</sup>, these

Element	$2p_{1/2}-1s_{1/2}$ intensity (%)	$2p_{3/2}-1s_{1/2}$ intensity (%)
$^{39}\text{K}$	14.25	28.49
$^{52}\text{Cr}$	16.20	32.40
$^{138}\text{Ba}$	25.02	50.03
$^{197}\text{Au}$	29.19	58.38

**Table 2.** Absolute calculated yields of the  $2p_{1/2}-1s_{1/2}$  and  $2p_{3/2}-1s_{1/2}$  transitions in muonic  $^{39}\text{K}$ ,  $^{52}\text{Cr}$ ,  $^{138}\text{Ba}$ ,  $^{197}\text{Au}$  after transfer in the gas cell.

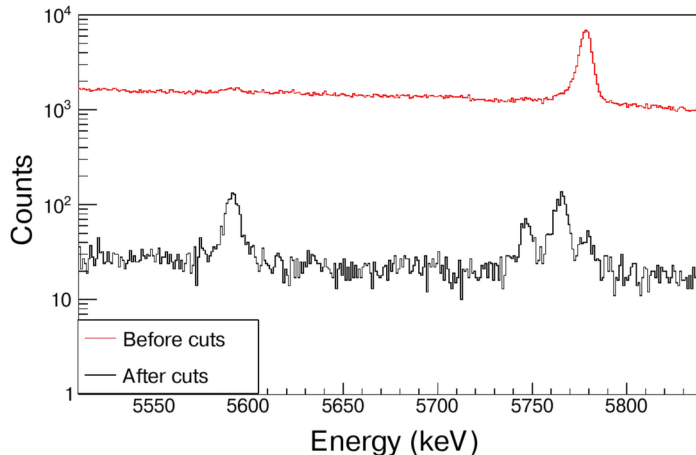


**Fig. 5.** Comparison of data before and after applying cuts. After cuts, the  $2p-1s$  signal of interest (5591 keV, 5746 keV, and 5765 keV) becomes substantially more prominent, while the continuous in time  $2p_{1/2}-1s$  of lead (at 5778 keV) is suppressed.

widths are estimated as  $\Gamma(K) = 0.5 \times 1.73 \times Z^{3.93} \times 10^{-6}\text{eV}$ . The significance of the choice of the refilling parameter in the cascade simulation was studied by halving or doubling its value or assuming no refilling of the K-shell at all. The findings show a relatively small change on the  $2p-1s$  yield ( $\sim 10\%$  relative deviation at most). The computed results for the  $2p_{3/2}-1s_{1/2}$  and  $2p_{1/2}-1s_{1/2}$  transition intensities are presented in Table 2. The summed  $2p-1s$  intensity of  $^{39}\text{K}$  (42.74%) corresponds well to the literature value of  $^{40}\text{Ar}$  (43.4(7)%)<sup>30</sup>, indicating that the calculations provide reasonable results.

### Analysis methods

Simulations in earlier works have shown that the maximum  $\mu d \rightarrow \mu Z$  atomic capture rate occurs for a deuterium concentration of around 0.25%. In this case, the distribution of events in time extends up to 500 ns after the muon enters the gas cell<sup>4</sup>. Applying a time cut with respect to the incoming muon, as well as some scintillator veto cuts, is critical to retrieve a good spectrum. Figure 5 shows a comparison between the total energy spectrum in the germanium detector, and the spectrum after cuts.

With regular fixed-threshold timing on germanium detectors, it becomes difficult to suppress background from uncorrelated and longer timescale events. In order to deal with this, extrapolated leading edge timing (ELET), as described in Ref.<sup>30</sup>, was employed, which allows for an improvement of the timing resolution by an order of magnitude. This method uses the leading edge trace of the waveform, to calculate a more accurate event time. The algorithm introduces two parameters, the threshold  $Th$  and the factor  $f$ . The time of the pulse is calculated using the crossings of the pulse waveform at  $Th$  and  $Th \times f$  above its baseline. The timestamps of these crossings are denoted as  $t_L$  and  $t_U$  and the time difference is defined as  $\Delta t = t_U - t_L$ . In this work, two ELET algorithms were used, which will be referred to as method A and method B. For these methods, the timing of a given event is calculated using Eqs. (1) and (2), respectively.

The former algorithm assumes that the time difference between the calculated ELET time and the lower threshold is equal to that of the lower threshold and the upper threshold. The latter algorithm performs an exact extrapolation to the baseline. Most detectors performed better under method A, which can be understood as a partial cancellation of non-linear behaviour between the two thresholds. Some detectors, notably BEGe detectors, performed substantially better using the exact extrapolation from method B in combination with lower thresholds. We believe this originates from the broader range of rise times, characteristic of the slow charge collection in these detectors. A graphical representation of both methods is shown in Fig. 6.

$$t_{ELET} = 2t_L - t_U = t_L - \Delta t, \text{ or} \quad (1)$$

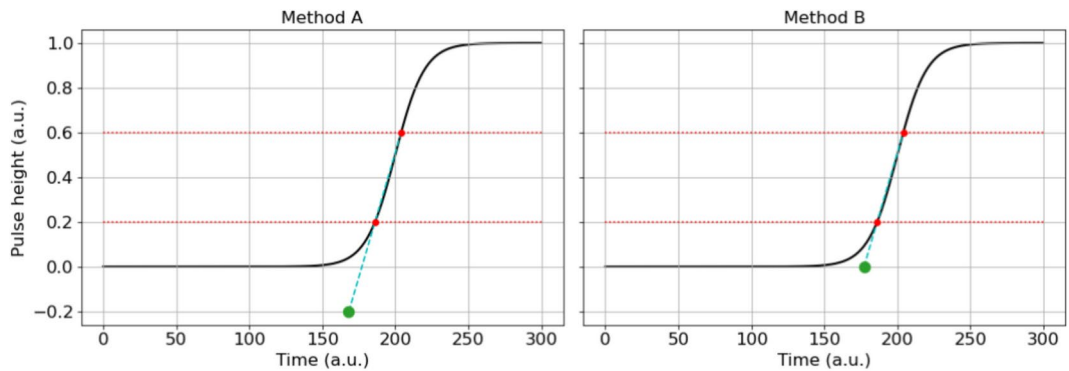


**Fig. 6.** Graphical representation of the two ELET algorithms applied in this work. The red dotted lines are the preset thresholds, which can be extrapolated using the cyan dashed lines to the predicted timestamp (green circle).

Element	Energy (keV)	Detection efficiency (%)
K 2p-1s	713	2.5(3)
Cr 2p-1s	1090	2.0(2)
Ba 2p <sub>1/2</sub> -1s	3923	0.62(7)
Ba 2p <sub>3/2</sub> -1s	3989	0.61(7)
Au 2p <sub>3/2</sub> -1s	5950	0.30(3)

**Table 3.** Total detection efficiency of the germanium detector array.

$$t_{ELET} = \frac{ft_L - t_U}{f - 1} = t_L - \frac{\Delta t}{f - 1} \quad (2)$$

To test the timing resolution for each set of parameters, the time difference spectrum of the germanium detector of interest is taken with respect to the muon entrance detector. Prompt muonic x rays are produced due to direct capture in parts of the setup, e.g., the titanium support grid of the gas cell. Hence, an energy cut can be taken around such a prompt line, which in this case was taken to be the 932 keV 2p-1s transition of titanium. After the optimization, the detectors were time aligned and the spectra were added, showing a FWHM of  $\sim 13.5$  ns.

It is well known that high-purity germanium detectors show a changing energy calibration over time due to fluctuations in temperature, humidity, and sudden changes to the setup such as vibrations. To counter these effects, calibration data was taken continuously during the measurement by placing sources in the setup. As conventional calibration sources do not reach up to the 2p-1s muonic x-ray lines of gold, isotopically pure <sup>208</sup>Pb was placed in front of the muon veto detector. This way, lead muonic x rays of known energy are emitted (described in Ref.<sup>31</sup>), such that they can be used for calibration purposes. To complement these, lines originating from some conventional calibration sources were used as well (<sup>22</sup>Na, <sup>60</sup>Co, and <sup>137</sup>Cs). The obtained data was used to recalibrate the detectors offline approximately every 8 hours, and whenever a new sample was placed in the setup.

The efficiency response function was investigated using similar techniques to those described in Ref.<sup>4,6,30</sup>. A 300  $\mu$ m-thick lead target was placed in the target position and was subsequently irradiated with muons. Assuming no scattering, all muons are captured such that the x-ray intensities are in principle known. Accordingly, one can calculate how many photons are emitted in each of the muonic x-ray transitions. Hence, the efficiency of the detector array can be evaluated. Due to previously observed discrepancies in the measured lead x-ray intensities, the literature x-ray intensities for gold were used<sup>32</sup>, which in previous work showed more consistent results<sup>4</sup>. Similar to the energy calibration, these were complemented with efficiency measurements using conventional sources (<sup>22</sup>Na, <sup>88</sup>Y, <sup>133</sup>Ba, and <sup>152</sup>Eu). The main difference, however, was that these could not be placed precisely in the target position. Hence, the efficiencies of these sources had to be rescaled to be in agreement with those calculated from the muonic lead lines. The statistical uncertainty on the efficiency fit indicated a statistical uncertainty on the order of a percent. A relative uncertainty of 10% was assumed for the efficiency, deemed conservative compared to systematic uncertainties originating from x-ray intensities and calibration source activities. The detection efficiencies in the regions of interest are given in Table 3.

Besides these photons detection efficiencies, the muon transmission efficiency through the entrance window was measured to be 55.1(11)%. This value is in good agreement with those observed in previous works<sup>4</sup>.

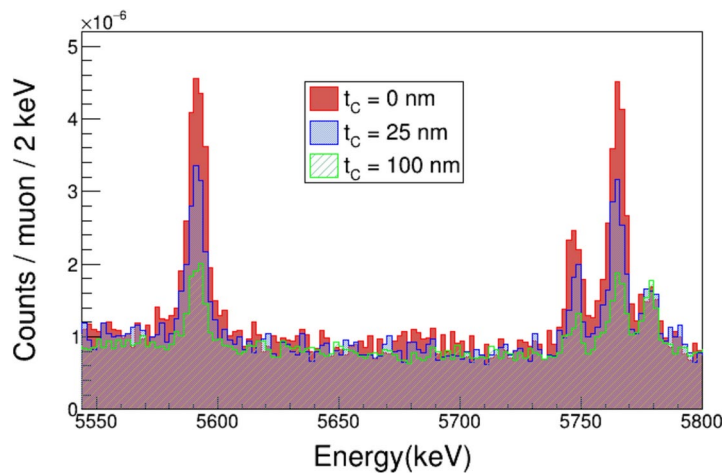


**Fig. 7.** Spectra obtained for gold samples with different graphite thicknesses. The  $2p_{-1}s$  signal of gold (5591 keV, 5746 keV, and 5765 keV) reduces with increasing graphite thickness ( $t_C$ ), while the  $2p_{1/2}-1s$  of lead (at 5778 keV) remains constant.

Graphite Thickness (nm)	$2p_{1/2}-1s$ count rate ( $10^{-6}$ muon $^{-1}$ )	$\Lambda_{tot}$ ( $10^{-3}$ muon $^{-1}$ )
0	16.9(7)	35.0(14)[42]
10	15.2(8)	31.5(16)[39]
25	10.7(6)	22.2(12)[28]
50	7.3(5)	15.1(10)[20]
100	4.9(3)	10.2(6)[14]
250	1.6(3)	3.23(44)[40]

**Table 4.** Gold muonic x-ray signal measured varying the thickness of the graphite coating covering the gold layer. The round brackets () represent the statistical error on the fit, while the square brackets [] represent the combined error of window transmission and detection efficiency.

## Results

To quantify the performance of the different samples, the atomic muon capture rate  $\Lambda_{tot}$ , and atomic capture rate per unit mass  $\Lambda_{mass}$  are calculated according to

$$\Lambda_{tot} = \frac{N_{det}}{N_\mu \epsilon_{det} \epsilon_T I_X}, \text{ and} \quad (3)$$

$$\Lambda_{mass} = \frac{\Lambda_{tot}}{m} \quad (4)$$

where  $N_{det}$  is the number of photons of a certain transition that were detected,  $N_\mu$  is the number of incoming muons,  $\epsilon_{det}$  is the photon detection efficiency,  $\epsilon_T$  is the window transmission,  $I_X$  is the relative yield (intensity) of the x ray of interest, and  $m$  the mass of the investigated target. The primary reason for quoting  $\Lambda_{mass}$  is to normalize for different target masses when making comparisons between different targets. The studied lines were those originating from the  $2p_{-1}s$  transitions.

## Attenuation in graphite

The range of  $\mu d$  atoms can be probed through the attenuation of the x-ray yield. The resulting measurements for this attenuation as a function of graphite layer thickness are shown in Fig. 7 and given in Table 4. For the measurements on gold, only the  $2p_{1/2}-1s$  transition was considered, as the  $2p_{3/2}-1s$  displays an only partially resolved hyperfine structure, and has significant overlap with peaks originating from the continuous  $^{208}\text{Pb}$  calibration. The resulting trend, shown in Fig. 8, is near-exponential with a half-value thickness of about 60 nm. This is in reasonable agreement with estimates made using the value obtained from the measured transfer rate for carbon of  $5 \times 10^{10} \text{ s}^{-1}$  at liquid hydrogen number density<sup>33,34</sup> after adjusting for the density of graphite (transfer rate of  $1.4 \times 10^{11} \text{ s}^{-1}$ ).

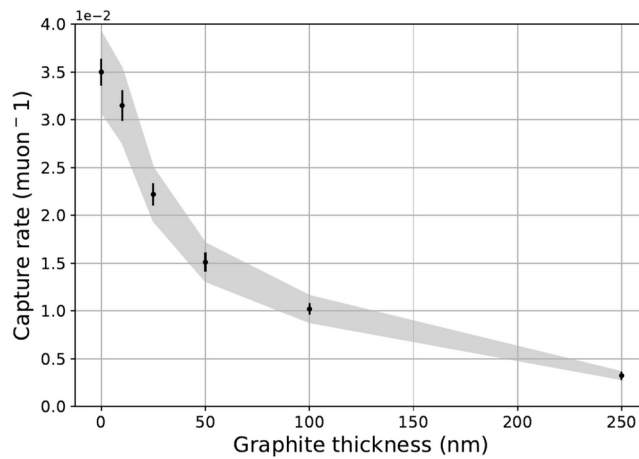


**Fig. 8.** Attenuation of the atomic capture rate as a function of graphite thickness. The error bars represent the statistical error and the grey band represents the systematic error on the measurements, which is the same relative factor for all data points ( $\sim 12\%$ ).

Target	Mass ( $\mu\text{g}$ )	$2p-1s$ count ( $10^{-6} \mu\text{on}^{-1}$ )	$\Lambda_{tot}$ ( $10^{-3} \mu\text{on}^{-1}$ )	$\Lambda_{mass}$ ( $10^{-3} \mu\text{on}^{-1} \mu\text{g}^{-1}$ )
$^{197}\text{Au}$ 10 nm	34.11	8.8(5)	18.3(11)[23]	5.4(4)[7]
$^{197}\text{Au}$ 3 nm	10.23	4.5(4)	9.3(8)[12]	9.1(8)[12]
$^{197}\text{Au}$ 90 keV	10.38	4.7(3)	9.7(5)[7]	9.4(5)[12]
$^{197}\text{Au}$ 27 keV	9.38	4.3(3)	8.8(6)[11]	9.4(7)[12]
$^{197}\text{Au}$ 4.5 keV	9.45	5.2(5)	11.6(10)[15]	12.3(10)[13]
$^{nat}\text{Cr}$ 25 nm	31.77	37.8(17)	7.7(4)[10]	2.42(11)[30]
$^{nat}\text{Cr}$ 4 nm	5.08	10.0(6)	2.04(11)[26]	4.0(2)[5]
$^{39}\text{K}$ 30 keV	7.20 *	12.4(3)	2.20(6)[27]	3.05(8)[38]
	4.16 <sup>†</sup>	12.4(3)	2.20(6)[27]	5.28(13)[64]

**Table 5.** Comparison of the measured signal between surface deposited (quoted by thickness) and implanted targets (quoted by implantation energy). The round brackets () represent the statistical error on the fit, while the square brackets [] represent the combined error of window transmission and detection efficiency. The targets with a quoted thickness are surface targets, while the one with quoted implantation energy are implanted targets. For the potassium, the mass near the surface (†) and the total mass (\*) are given.

### Implanted targets

Using similar calculations, the gold and potassium implanted targets were compared to surface deposition targets. For potassium and chromium, the fine structure could not be fully resolved. Hence, the  $2p-1s$  peak was fitted with a double Gaussian. The results are shown in Table 5. As the outer parts of the target disks are covered by the sample holder, quoted target masses only include the inner 15 mm diameter. As mentioned before, only about 60% of the particles are located near the surface of the substrate for the implanted  $^{39}\text{K}$  target. Accordingly, both the total mass and the part near the surface are quoted, marked by an asterisk (\*) and a dagger (†) in Table 5, respectively.

In order to compare different samples, the atomic capture rate is used. Targets with a higher mass typically have a higher  $\Lambda_{tot}$ , as more particles are present, but this does not provide a good indication to the quality of a sample. In contrast, if masses are similar,  $\Lambda_{mass}$  is a good comparison when trying to determine which target preparation method is better. Another important note is that the atomic capture rate depends on the spacial extent of the Coulomb potential. Hence, the ratio of atomic capture rates between medium-Z and high-Z targets are listed separately. If we thus compare the implanted targets of similar atomic number and mass, we see that the difference in capture rate is at most  $\mathcal{O}(10\%)$ . The implanted targets performed equally well as surface targets, showing there are only limited losses to the substrate material. This result indicates that implantation offers a good alternative target fabrication strategy for muonic atom experiments with microgram targets.

### Chemically prepared targets

Finally, a comparison was made between barium targets produced via MP and DoD printing. For barium, the fine structure is fully resolved, such that its components can be fitted individually. The samples produced through MP showed a significantly larger signal for the same target mass than those prepared through DoD printing. Even the 50  $\mu\text{g}$  DoD printed target did not show a clear signal. By fixing the energy positions and

Target	2p-1s count rate ( $10^{-6}$ muon $^{-1}$ )	$\Lambda_{tot}^{-4}$ muon $^{-1}$	$\Lambda_{mass}$ ( $10^{-6}$ muon $^{-1}\mu\text{g}^{-1}$ )
MP 25 $\mu\text{g}$	15.4(9)	61.0(4)[8]	24.2(13)[30]
MP 10 $\mu\text{g}$	9.8(6)	39(3)[5]	39(3)[5]
MP 5 $\mu\text{g}$	6.4(6)	25(3)[4]	51(5)[7]
DoD 50 $\mu\text{g}$	1.8(5)	7.1(18)[9]	1.42(36)[18]
DoD 25 $\mu\text{g}$	< 1.05	< 4.1[5]	< 1.6[3]
DoD 10 $\mu\text{g}$	< 1.46	< 5.7[7]	< 5.7[7]

**Table 6.** Barium muonic x-ray signal measured using different fabrication strategies and target masses. The round brackets () represent the statistical error on the fit, while the square brackets [] represent the combined error of window transmission and detection efficiency.

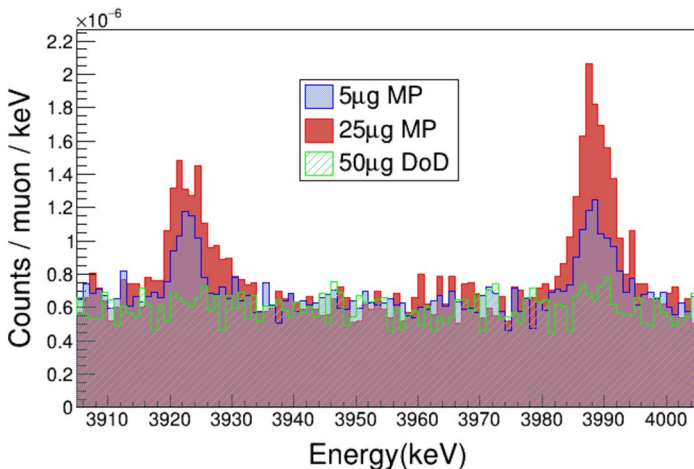


**Fig. 9.** Comparison of spectra obtained by measuring different barium targets showing the  $2p_{1/2}-1s$  (3923 keV) and  $2p_{3/2}-1s$  (3989 keV) transitions. The molecular plated (MP) targets had a substantially higher signal than the drop-on-demand (DoD) targets.

relative intensities of the two fine structure peaks, it was possible to extract a non-zero  $\Lambda_{tot}$  for the 25  $\mu\text{g}$  MP sample. For the other two DoD printed samples, only an upper limit could be extracted. The results are given in Table 6 and a comparison of the spectra is shown in Fig. 9. The lower atomic capture rates in the DoD printed samples are suspected to be caused by organic surface contamination originating from the solutions used in the target making process/contact with air, or by clustering of barium on the substrate, thus greatly reducing the active surface.

It is rather difficult to make a quantitative comparison between the barium targets and the implanted gold and potassium targets, as transfer rates depend on the atomic number and the needed scattering cross sections for  $\mu\text{d}$  atoms in these materials are not well known. Given that barium has atomic number  $Z = 56$ , one would expect that its atomic capture rate per unit mass would be substantially closer to that of gold ( $Z = 79$ ) than that of potassium ( $Z = 19$ ). However, even for the best  $\Lambda_{mass}$  (5  $\mu\text{g}$  MP sample), it is only comparable to that of the implanted potassium and thus about half of the one for gold. This is not unexpected as the barium is deposited in molecular form and some organic contamination is codeposited during the process thus leading to additional muon losses. However, these results also show that good x-ray yields can be achieved from such chemical target preparation methods (given a uniform deposition and low amount of organic contamination) when implantation or surface deposition is not an option.

## Conclusion

A systematic study was performed to investigate the most appropriate target preparation techniques for microgram muonic atom spectroscopy. The range of  $\mu\text{d}$  atoms in carbon was probed by measuring the x-ray yield with different thicknesses of graphite coating on gold. The resulting trend shows a near-exponential behavior with a half-value thickness of approximately 60 nm, which is in reasonably good agreement with first order estimates based on the transfer rate of carbon. This shows the importance of minimizing organic surface layers originating from the solutions used for chemical preparation or contact with air, which may reduce the quality of reactive species, such as radium. The range of  $\mu\text{d}$  atoms also indicates the feasibility of using implanted targets, which was in turn tested successfully by measurement of implanted gold and potassium targets. An additional benefit of implantation is the enhanced protection of chemically reactive species. However, an important

factor remains the effect of self-sputtering for larger implanted quantities, which needs to be controlled. These sputtering simulations are discussed in more detail in our earlier work<sup>17</sup>. Finally, our findings show that targets with good x-ray yield can also be prepared by chemical deposition methods, such as molecular plating, when a uniform deposition with low organic contamination can be achieved.

This work has shown the viability of using implanted targets for microgram muonic atom spectroscopy, and paves the way to future measurements using this approach, e.g. the measurement of the <sup>39, 40, 41</sup>K triplet, where magnetic mass separation using an ion beam is a must.

## Data availability

The datasets generated for and/or analysed during the current study are available from the corresponding author on reasonable request.

Received: 9 August 2024; Accepted: 17 February 2025

Published online: 26 February 2025

## References

1. Yang, X., Wang, S., Wilkins, S. & Ruiz, R. G. Laser spectroscopy for the study of exotic nuclei. *Prog. Part. Nucl. Phys.* **129**, 104005 (2023).
2. Fricke, G. et al. Nuclear ground state charge radii from electromagnetic interactions. *At. Data Nucl. Data Tables* **60**, 177–285 (1995).
3. Tsukada, K. et al. First observation of electron scattering from online-produced radioactive target. *Phys. Rev. Lett.* **131**, 092502 (2023).
4. Adamczak, A. et al. Muonic atom spectroscopy with microgram target material. *Eur. Phys. J. A* **59**, 15 (2023).
5. Mulhauser, F. et al. Ramsauer–Townsend effect in muonic atom scattering. *Phys. Rev. A* **73**, 034501 (2006).
6. Vogiatzi, S. M. Studies of muonic <sup>185,187</sup>Re, <sup>226</sup>Ra, and <sup>248</sup>Cm for the extraction of nuclear charge radii. Ph.D. thesis, ETH Zurich (2023).
7. Mauger, E. et al. Preparation of <sup>7</sup>Be targets for nuclear astrophysics research. *J. Instrum.* **12**, P02016 (2017).
8. Parker, W. & Falk, R. Molecular plating: A method for the electrolytic formation of thin inorganic films. *Nucl. Instrum. Methods* **16**, 355–357 (1962).
9. Vascon, A. et al. Elucidation of constant current density molecular plating. *Nucl. Instrum. Methods Phys. Res. Sect. A* **696**, 180–191 (2012).
10. Renisch, D. et al. Actinide and lanthanide thin-layer developments using a drop-on-demand printing system. In *EPJ Web of Conferences*, Vol. 285, 04001 (2023).
11. Grillenberger, J., Baumgarten, C. & Seidel, M. The high intensity proton accelerator facility. *SciPost Phys. Proc.* **5**, 002 (2021).
12. Gerchow, L. et al. Germanium array for non-destructive testing (GIANT) setup for muon-induced x-ray emission (MIXE) at the Paul Scherrer Institute. *Rev. Sci. Instrum.* **94**, 045106 (2023).
13. Warr, N. et al. The miniball spectrometer. *Eur. Phys. J. A* **49**, 1–32 (2013).
14. Kosztorús, Á. et al. Charge radii of exotic potassium isotopes challenge nuclear theory and the magic character of N=32. *Nat. Phys.* **17**, 439–443 (2021).
15. Wauters, F. & Knecht, A. The muX project. *SciPost Phys. Proc.* **5**, 022 (2021).
16. Ziegler, J. F., Ziegler, M. D. & Biersack, J. P. SRIM—the stopping and range of ions in matter (2010). *Nucl. Instrum. Methods Phys. Res. Sect. B* **268**, 1818–1823 (2010).
17. Heines, M. et al. Muonic x-ray spectroscopy on implanted targets. *Nucl. Instrum. Methods Phys. Res. Sect. B* **541**, 173–175 (2023).
18. Gamer, L. et al. Simulation and optimization of the implantation of holmium atoms into metallic magnetic microcalorimeters for neutrino mass determination experiments. *Nucl. Instrum. Methods Phys. Res. Sect. A* **854**, 139–148 (2017).
19. Möller, W. & Eckstein, W. Tridyn—a TRIM simulation code including dynamic composition changes. *Nucl. Instrum. Methods Phys. Res. Sect. B* **2**, 814–818 (1984).
20. Akyolas, V. & Vogel, P. Muonic atom cascade program. *Comput. Phys. Commun.* **15**, 291–302 (1978).
21. Bearden, J. A. & Burr, A. F. Reevaluation of x-ray atomic energy levels. *Rev. Mod. Phys.* **39**, 125–142 (1967).
22. Cardona, M. & Ley, L. (eds) *Photoemission in Solids I: General Principles* (Springer, Berlin, Heidelberg, 1978).
23. Fuggle, J. C. & Mårtensson, N. Core-level binding energies in metals. *J. Electron Spectrosc. Relat. Phenom.* **21**, 275–281 (1980).
24. Clementi, E. & Raimondi, D. L. Atomic screening constants from SCF functions. *J. Chem. Phys.* **38**, 2686–2689 (1963).
25. Clementi, E., Raimondi, D. L. & Reinhardt, W. P. Atomic screening constants from SCF functions. II. Atoms with 37 to 86 electrons. *J. Chem. Phys.* **47**, 1300–1307 (1967).
26. Sturniolo, S. & Hillier, A. Mudirac: A Dirac equation solver for elemental analysis with muonic X-rays. *X-Ray Spectrom.* **50**, 180–196 (2021).
27. Haff, P., Rodrigo, E. & Tombrello, T. Muon transfer in gas targets. *Ann. Phys.* **104**, 363–379 (1977).
28. Bambrynek, W. et al. X-ray fluorescence yields, Auger, and Coster–Kronig transition probabilities. *Rev. Mod. Phys.* **44**, 716–813 (1972).
29. Vogel, P. Atomic aftereffects and the line shape of muonic X rays. *Phys. Rev. A* **8**, 2292–2297 (1973).
30. Skawran, A. Development of a new method to perform muonic atom spectroscopy with microgram targets. Ph.D. thesis, ETH Zurich (2021).
31. Bergem, P. et al. Nuclear polarization and charge moments of <sup>208</sup>Pb from muonic x rays. *Phys. Rev. C* **37**, 2821 (1988).
32. Hartmann, F. et al. Measurement of the muonic x-ray cascade in Mg, Al, In, Ho, and Au. *Zeitschrift für Physik A Atoms and Nuclei* **305**, 189–204 (1982).
33. Dupays, A. Muon transfer from muonic hydrogen to carbon. *Phys. Rev. A* **72**, 054501 (2005).
34. Basiladze, S., Ermolov, P. & Oganessian, K. Measurement of the rate of transfer of a muon from a pμ atom to nuclei of other elements. *Soviet J. Exp. Theor. Phys.* **22**, 725 (1966).

## Acknowledgements

The experiments were performed at the πE1 beam line of PSI. We would like to thank the accelerator and support groups for the excellent conditions. Additional technical support by F. Barchetti, F. Burri, M. Hildebrandt, M. Meier, L. Noorda, and A. Stoykov from PSI is gratefully acknowledged. We thank the PSI laboratories LNQ and LIN - especially A. Weber and H. Kovacikova - for the preparation of the sputtered and evaporated targets. The germanium detector setup is shared with the MIXE project at PSI (<https://www.psi.ch/en/smus/muon-induced-x-ray-emission-mixe-project>), who have greatly contributed to its construction, providing a fantastic plat-

form for several muonic atom experiments taking place at PSI. The authors thank Ernst Artes and Carl-Cristian Meyer for their help in the production and characterization of the DoD targets.

### Author contributions

L.A., T.E.C., J.F., M.H., R.H., U.K., T.K., L.P., and A.V. were involved in the making and characterizing of the implanted samples. C.B., C.E.D., and D.R. made the DoD samples. E.A.M. made the MP samples. S.B., T.E.C., M.H., P.I., K.K., A.K., M.N., A.O., R.P., N.R., K.v.S., S.M.V., F.W., and S.Z. contributed to the data collection. T.E.C., M.H., A.K., S.M.V., and K.v.S. were involved in the analysis. T.E.C., M.D., A.D., M.H., P.I., K.K., A.K., E.A.M., W.W.M.M.P., R.P., K.v.S., S.M.V., F.W., and A.Z. were involved in discussing the results. M.H. wrote the manuscript, and all co-authors reviewed it.

### Funding

The authors want acknowledge the following funding institutions. The Swiss National Science Foundation, Sinergia project “Deep $\mu$ ”, Grant: 193691 (MIXE); FWO Vlaanderen, through proposal numbers G0G3121N (NSHAPE), 1167324N (S. Bara) and 11P6V24N (M. Deseyn); KU Leuven BOF under contract number C14/22/104; the European Research Council (ERC) through proposal number 101088504 (NSHAPE); The RADIATE programme under the Grant Agreement 824096 from the EU research and Innovation programme HORIZON 2020 (proposal 22002733-ST and 22002894-ST); The EPSRC under contract number EP/X015491/1; the ETH Research Grant 22-2 ETH-023 (K. von Schoeler); Center of Excellence in High energy Physics and Astrophysics, Suranaree University of Technology.

### Declarations

#### Competing interests

The authors declare no competing interests.

#### Additional information

**Correspondence** and requests for materials should be addressed to M.H.

**Reprints and permissions information** is available at [www.nature.com/reprints](http://www.nature.com/reprints).

**Publisher’s note** Springer Nature remains neutral with regard to jurisdictional claims in published maps and institutional affiliations.

**Open Access** This article is licensed under a Creative Commons Attribution-NonCommercial-NoDerivatives 4.0 International License, which permits any non-commercial use, sharing, distribution and reproduction in any medium or format, as long as you give appropriate credit to the original author(s) and the source, provide a link to the Creative Commons licence, and indicate if you modified the licensed material. You do not have permission under this licence to share adapted material derived from this article or parts of it. The images or other third party material in this article are included in the article’s Creative Commons licence, unless indicated otherwise in a credit line to the material. If material is not included in the article’s Creative Commons licence and your intended use is not permitted by statutory regulation or exceeds the permitted use, you will need to obtain permission directly from the copyright holder. To view a copy of this licence, visit <http://creativecommons.org/licenses/by-nc-nd/4.0/>.

© The Author(s) 2025